

Investigation of Thermal Mixing in the Control Rod Top Tube Using Large Eddy Simulations

R. Pegonen^{a,*}, N. Edh^b, K. Angele^c, H. Anglart^a

^a*KTH Royal Institute of Technology, Roslagstullsbacken 21, SE-10691 Stockholm, Sweden*

^b*Forsmarks Kraftgrupp AB, SE-74203 Östhammar, Sweden*

^c*Vattenfall Research & Development AB, SE-81426 Älvkarleby, Sweden*

Abstract

Thermal mixing and thermal fatigue has led to component failures in the nuclear industry. The thermal fatigue phenomenon is intimately linked with the mixing of streams of different temperatures in proximity to a solid wall. Due to conjugate heat transfer, temperature fluctuations are induced in the wall. One of the key issues is to predict the amplitude and the frequency of the fluctuations. This paper presents pre-calculations of the thermal mixing experiments that are under preparation at the KTH Royal Institute of Technology as part of the THEMFE project (Thermal Mixing and Fatigue Experiment).

The proposed geometry is a simplification of a reactor control rod and consists of a top-tube and control rod stem, which are modeled as concentric cylinders. In addition there are only two hot inlet jets and two cold inlet jets, whereas in reality there are 8 upper inlets and 4 lower inlets for hot bypass water and the cold flow is annular.

Thermal mixing was studied by using a transient Computational Fluid Dynamics (CFD) solver for the incompressible filtered Navier-Stokes equations and employing a Large Eddy Simulation model of turbulence implemented in OpenFOAM. The aim was to verify that the proposed simplified geometry and the flow conditions of the experiment will lead to low frequent temperature fluctuations of the order of 0.1-1 Hz, as seen in previous experiments with the real geometry. Such low frequencies are typical for the thermal fatigue phenomenon. The study was focused on the region near the control rod stem and therefore a refined grid was used in that region. The final mesh consisted of over one million cells.

The results did indeed reveal low frequent temperature fluctuations in the lower part of the mixing region near the control rod stem. The results of this paper indicate that the length of the mixing region is 23 cm, which is large enough to be resolved in the experiment. It was also found that the most dangerous region, where the dominant high amplitude temperature fluctuations have a frequency of the order of 0.1 Hz, is 4 cm long. As expected, the instant flow field is asymmetric with large secondary flows. The present results verify that the proposed geometry and flow conditions can be applied in the experiment.

Keywords: Thermal mixing, Mixing region, Low frequency temperature fluctuations, Computational Fluid Dynamics, Large Eddy Simulation, Incompressible flow

1. Introduction

Turbulent mixing of two streams with different temperature can cause temperature fluctuations that may lead to thermal fatigue. Thermal fatigue has received increasing attention in recent years in the nuclear industry due to component failures. Control rod drive problems were observed during the refueling outage of Unit 3 of Oskarshamn Nuclear Power Plant in Sweden in October 2008 [1, 2]. A crack was discovered in the welded joint at the control rod stem [2]. This led to inspections by the Swedish Radiation Safety Authority of all other control rods at Oskarshamn 3 and at its "twin" reactor Forsmark 3. Results from Forsmark 3 revealed that about 25% of the 197 checked control rod drives were found to have crevices or relevant cracks and one was broken [1]. The cracks that were found in the upper part of the stem of many control rods originated from thermal fatigue caused by the mixing of cold laminar crud flow in the annular gap between the control rod stem and the top tube (60°C) and hot turbulent bypass flow (276°C), forming jets through holes in the guide tube [2].

This paper presents pre-calculations of the thermal mixing experiments that are under preparation at the KTH Royal Institute of Technology as part of the THEMFE project. The aim of THEMFE is to obtain experimental data to predict heat transfer. These data are to be used to benchmark CFD calculations. The aim of this work was to make preparatory simulations for the experiment using the open-source CFD code OpenFOAM. The geometry in THEMFE is simplified control rod, top-tube and guide tube geometry with only two upper and two lower by-pass inlets. The complex geometry of a control rod is significantly simplified. The geometry used in this work was simplified further, in order to focus on the mixing region. All the simplifications were done in a way to preserve the relevant physics of the thermal mixing. The goal of these simulations was to verify that the proposed geometry would give rise to low frequent fluctuations (of the order of 0.1...1 Hz). These fluctuations are considered to be responsible

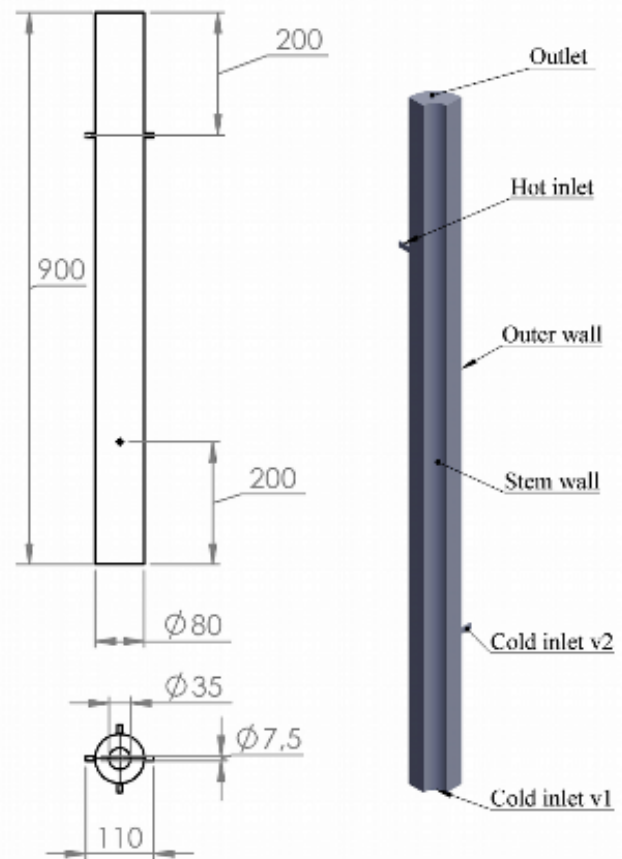


Figure 1: (Left) Dimensions (in millimeters) of the second case geometry; (right) nomenclature on the quarter geometry

for the control rod drive thermal fatigue and the results of this work were used for deciding on the experimental setup and experimental conditions.

Previous CFD simulations done in Forsmark on the real control rod geometry showed that the temperature fluctuates in the mixing region with a frequency varying from 0.01 Hz to 1 Hz and that the fluctuations are triggered by eddies coming from the upper warm water bypass flow inlets [2, 3].

2. Computational Model

2.1. Geometry

The design of the geometries used in this work was based on the configuration that was proposed as a test section in the THEMFE experiment. The current simulation geometries covered the part of the total test section where temperature fluctuations were expected. In this work two separate geometries were

*Corresponding author

Email address: pegonen@kth.se (R. Pegonen^{a,*})

considered. The detailed dimensions can be found in Fig. 1. The difference between the first and the second case geometry was the position of the cold flow inlets (60°C). In the first case water was coming in through the annulus located at the bottom of the geometry, see cold inlet $v1$ marked in Fig. 1, but there were no inlets on the sides. In the second case there were inlets on the sides, but no inlet at the bottom annulus, see cold inlet $v2$ marked in Fig. 1. The second case geometry is similar to the geometry that will be used in the THEMFE experiment. The purpose of having two different geometries was to see the effect of the cold jets on the mixing region. In both cases the mass flow through the hot and cold inlets was 0.8 kg/s and 0.07 kg/s, respectively.

2.2. Mesh

One multi-block hexahedral grid was constructed for each case. The advantage of using hexahedral cells over tetrahedral cells is that for the same cell count, hexahedral meshes will give a less diffusive solution compared to the one with tetrahedral cells, especially if the grid lines are aligned with the flow. Furthermore, hexahedral cells need less than half the nodes to provide the same physical resolution as in the case of the tetrahedral mesh [4].

In multi-block grid generation, the geometry is first divided into smaller blocks which are thereafter separately meshed using structured mesh generation. A structured mesh is commonly built from hexahedra by repeating its geometrical and topological structure [5].

In both cases one quadrant of full geometry was meshed and thereafter the mesh was mirrored twice to obtain the full 360° mesh. This approach was used to ensure the mesh would be symmetrical. Both grids contained only hexahedral cells and the total number of cells is presented in Table 1. The number of cells was picked to have enough refinement to ensure accurate results while being coarse enough to limit the required computing time. The Courant-Friedrichs-Lewy condition [6, 7]:

$$Co = \frac{v\Delta t}{\Delta x} \leq 0.5, \quad (1)$$

was used when deciding on the cell lengths, Δx . By estimating velocities v and by fixing the time step

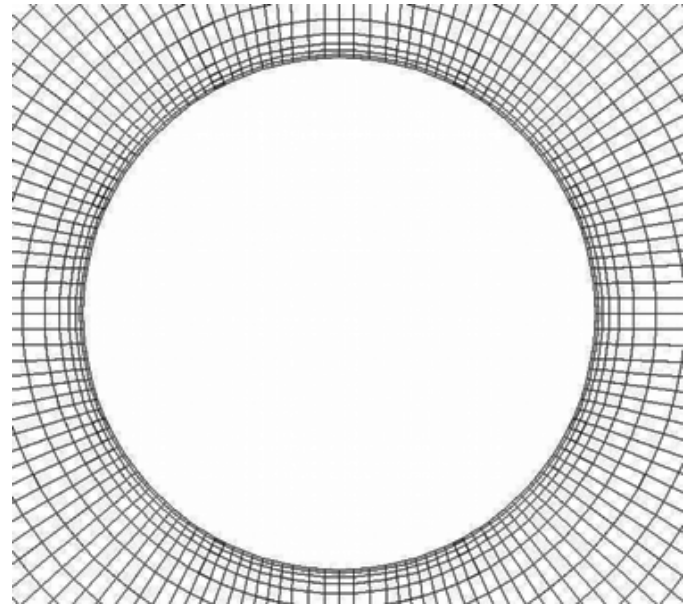


Figure 2: Zoomed top view of the mesh (Mesh is refined near the stem wall to get more accurate results in the most interesting area)

value, Δt .

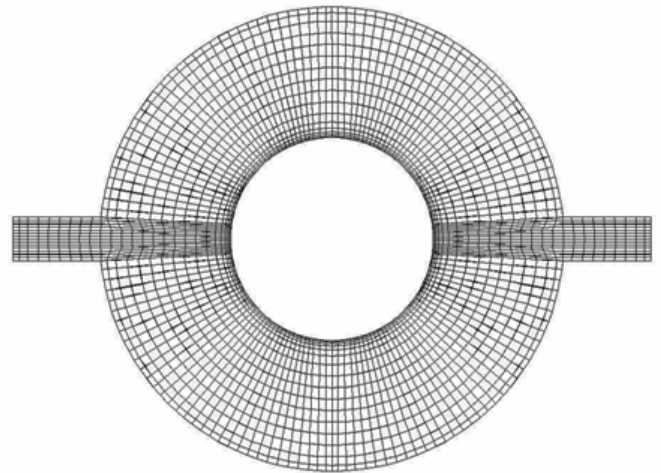


Figure 3: Cut view of the inlets as viewed from above

In both cases the maximum element size was defined to be 2 mm. The minimum element size was chosen globally to be 1 mm except for near the control rod stem wall (0.2 mm) and the expansion ratio was adjusted to 1.5. Refinement on the control rod stem wall (Fig. 2) was done in order to get more accurate results in the most interesting area—near the control rod stem. Additional refinement had to be done near the inlets (Figs 3...4) because otherwise the inlet flow would not have been accurate.

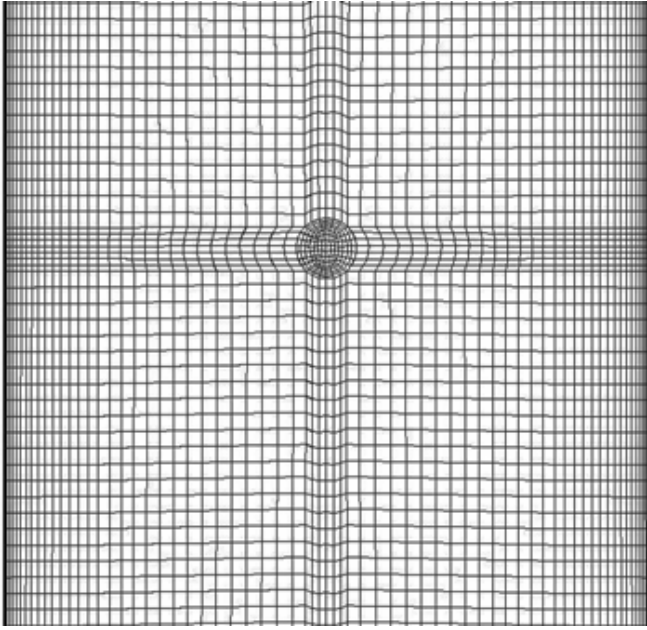


Figure 4: Side view of the mesh

To have enough cells to accurately represent the inlet profile, to have roughly the same cell sizes in the inlet pipes as in the mixing region and to keep high mesh quality, meshing had to be done in a way to reduce inaccuracies that might originate from the effect of local refinement: the flow can have an unphysical non-equilibrium state when it moves between regions with different cell sizes [7]. In other words we could expect to see abrupt changes in solutions on the borders of the refinement regions.

The meshing quality was improved by using O-Grid blocking to reduce the skewness where a block corner lies on a continuous curve or surface (Outer wall, Stem wall and outer walls of the inlets in Fig. 1). It arranges the grid lines into an "O" shape.

One of the parameters that describe quality of the mesh is skewness. For hexahedral elements, skewness is defined as the normalized worst angle between each of the six face normals and the vector defined by the centroid of the hexahedron and the center of the face [8]. The skewness is normalized so that "1" denotes the ideal case and "0" the worst possible case. Both cases had skewness above 0.75 and most of the cells above 0.95 (see Table 1).

To study the influence of mesh size on the results, three different test cases with hexahedral grids (533,368, 1,029,636 and 2,139,184 cells) were con-

Table 1: Mesh information

	Mesh 1	Mesh 2
Points	1,096,456	1,146,256
Cells	1,029,636	1,076,360
Faces	3,155,570	3,298,796
Internal Faces	3,022,246	3,159,364
Hexahedra	1,029,636	1,076,360
Boundary patches	6	7
Max volume of cell (mm ³)	8	8
Skewness > 0.95, %	99.3	98.9

structed in a similar way, as described above, and were compared in the same conditions. The first case geometry was used and 8.5 s of LES transient simulation results were obtained. For the comparison, mean temperatures as well as temperature standard deviation 1 mm from the stem were calculated while using probe data from all four locations, see Fig. 5. It was observed that the vertical location and the length of the mixing region remained nearly the same. In addition it was seen that by improving the mesh the "peak" of the temperature standard deviation is sharper and moves vertically upwards and the mean temperature has its steepest rise vertically upwards. In the region where low frequency temperature oscillations occur ($y \approx 0.39$ m) the difference between mean temperatures is below 10 degrees (4.6% temperature difference between hot and cold inlet), when comparing the two finest cases. Although a grid with 2,139,184 cells would give the most accurate results, it is prohibitively "expensive" for use in the simulation and would take 5 months of computing time (utilizing 208 processor cores), which could not be afforded in this work. Therefore a grid containing 1,029,636 cells was used during these simulations.

2.3. The Choice of Turbulence Model

2.3.1. RANS and LES

The Navier-Stokes equations for incompressible Reynolds-averaged (or spatially filtered) turbulent flows can be written as [9]:

$$\frac{\partial \bar{v}_i}{\partial x_i} = 0, \quad (2)$$

$$\frac{D\bar{v}_i}{Dt} = -\frac{1}{\rho} \frac{\partial \bar{p}}{\partial x_i} + \frac{\partial}{\partial x_j} \left[\nu \frac{\partial \bar{v}_i}{\partial x_j} - \tau_{ij}^{R/SGS} \right] + \bar{f}_i, \quad (3)$$

where ν is the velocity, ρ is the density, p is the pressure, ν is the molecular kinematic viscosity and f is the total body acceleration. Overline represents either Reynolds-averaging (or spatial filtering). $\tau_{ij}^{R/SGS}$ is respectively Reynolds (or sub-grid-scale (SGS)) stress tensor and it can be evaluated by using the Boussinesq assumption (taken into account incompressibility) [10]:

$$\tau_{ij}^{R/SGS} = -\nu_{t/SGS} \bar{S}_{ij} + \frac{2}{3} k_{t/SGS} \delta_{ij}, \quad (4)$$

where $\nu_{t/SGS}$ is the turbulence (or SGS) kinematic viscosity, $k_{t/SGS}$ is the specific turbulent (or SGS) kinetic energy and S_{ij} is rate-of-strain tensor.

There are many different models to calculate ν_t used in RANS. One possibility is to use the standard $k-\epsilon$ model, where ν_t is expressed as [11]:

$$\nu_t = C_\mu \frac{k_t^2}{\epsilon}, \quad (5)$$

and to close unknown variables k_t and ϵ [10]:

$$\frac{Dk_t}{Dt} = \frac{\partial}{\partial x_j} \left(\left(\nu + \frac{\nu_t}{\sigma_k} \right) \frac{\partial k_t}{\partial x_j} \right) + \nu_t \bar{S}^2 - \epsilon, \quad (6)$$

$$\frac{D\epsilon}{Dt} = \frac{\partial}{\partial x_j} \left(\left(\nu + \frac{\nu_t}{\sigma_\epsilon} \right) \frac{\partial \epsilon}{\partial x_j} \right) + \frac{C_{\epsilon 1} \nu_t \bar{S}^2 \epsilon}{k_t} - \frac{C_{\epsilon 2} \epsilon^2}{k_t}, \quad (7)$$

here ϵ denotes the kinetic energy dissipation rate, $C_\mu = 0.09$, $C_{\epsilon 1} = 1.44$, $C_{\epsilon 2} = 1.92$, $\sigma_k = 1.0$, $\sigma_\epsilon = 1.3$ and $S = \sqrt{2S_{ij}S_{ij}}$.

If the One Equation Eddy model is used in LES then ν_{SGS} is given by [10]:

$$\nu_{SGS} = (C_S \bar{\Delta})^2 \bar{S}, \quad (8)$$

here $C_S \approx 0.16$ and $\Delta = \sqrt[3]{\Delta_1 \Delta_2 \Delta_3}$ (Δ_i —filter size in the i -th spatial coordinate). To close unknown k_{SGS} [10]:

$$\frac{Dk_{SGS}}{Dt} = \frac{\partial}{\partial x_j} \left(\nu_{eff} \frac{\partial k_{SGS}}{\partial x_j} \right) + \nu_{SGS} \bar{S}^2 - \frac{C_\epsilon k_{SGS}^{\frac{3}{2}}}{\bar{\Delta}}, \quad (9)$$

here $\nu_{eff} = \nu + \nu_{SGS}$ and $C_\epsilon \approx 1.05$.

When the Smagorinsky model is used then ν_{SGS} and k_{SGS} are modeled as [10]:

$$\nu_{SGS} = (C_S \bar{\Delta})^2 \bar{S}, \quad (10)$$

$$k_{SGS} = 2 \frac{C_k}{C_\epsilon} \bar{\Delta}^2 \bar{S}^2, \quad (11)$$

here $C_S \approx 0.16$ and $C_k \approx 0.07$.

2.3.2. The Choice

Three turbulence models, one RANS and two LES models, were considered and comparative simulations were carried out for the choice of model. The standard $k-\epsilon$ approach was used in RANS; in LES the One Equation Eddy and Smagorinsky models were tested. The geometry created for the choice of turbulence model was similar to that seen in Fig. 1, but it was 200 mm shorter (700 mm instead of 900 mm). The mesh had 475,376 hexahedral cells and was created as discussed above.

With RANS, in order to set fully-developed velocity profiles for the inlets a steady state precursory calculation was carried out on a straight pipe with a length of 20 diameters. The results of the precursory simulation were mapped on to the inlets before the PIMPLE (merged PISO-SIMPLE) algorithm was used for the transient simulation [12–14]. The RANS transient simulation was carried out on 16 processor cores and 10.97 s of simulation time was achieved within 7 days.

With LES the PISO algorithm was used and two cases were constructed which differed in respect of the LES models used: the One Equation Eddy model and the Smagorinsky model. Flat inlet flow conditions were applied because the steady-state algorithm cannot be used with LES. The Smagorinsky LES model reached 42.6 s simulation time within 19 days while using 32 processor cores, whereas the One Equation Eddy model reached only 30.2 s.

After the results were analyzed, LES was selected for use in the final case. There were two main reasons for that: the RANS averaged out momentum and temperature fluctuations, therefore these could not be observed; both LES versions showed similar behaviors. In [15] a comprehensive literature study concerning thermal mixing in T-junctions is presented in addition to new results. The literature study strengthens the hypothesis that LES is expected to make a better prediction of the mixing region:

”The most notable advantage of LES model over RANS models is that the former can depict the detailed process of the generation, development and disappearance of various vortexes of turbulent flow

in transient state.” [15]

Although the One Equation Eddy and the Smagorinsky models gave similar results the Smagorinsky was preferred, because it was 1.5 times faster than the One Equation Eddy model. That can be explained by the fact that the One Equation Eddy model has one more transport equation to solve. In conclusion, the Smagorinsky model was chosen and during the final simulations 208 processor cores were utilized and 75 s were simulated in 1,200 CPU hours.

2.4. CFD Simulation

In this work all CFD simulations were carried out by using the free, open source CFD toolbox called OpenFOAM, version 2.0.x. The current work needed a transient solver that would take into account buoyancy effect, heat transfer, single-phase incompressible flow and use an LES model. The solver that was used is called buoyantBoussinesqGenPisoFoam and it is based on OpenFOAMs standard solver buoyantBoussinesqPisoFoam [16, 17]. The solver used differs from the standard one in the respect that it uses the LES library, whereas the standard one only uses the RANS library. The boundary conditions used are shown in Table 2.

- fixedValue—The fixed value boundary condition defines Φ to have a value Φ_b on boundary b [18],
- zeroGradient—The normal gradient of Φ on boundary b is zero [7],
- inletOutlet—zeroGradient is applied to all faces on boundary b , except for those where there is inflow, in which case fixedValue is used [12],
- calculated—Boundary field Φ is calculated by using other fields [12],
- WallFunction—Empirical function for obtaining suitable conditions near the wall without having extremely refined grid,

- radialProfile—Radial profile boundary condition defines Φ to have user specified radially symmetric profile on boundary b [16].

Velocity profiles for the small inlets were obtained by rescaling earlier measurement results done in different conditions [19]. Rescaling was done in such a way as to fit the velocity profile to the current geometry and to have the right mass flow. The obtained flow is not perfect, but it was preferred to a "flat" inlet velocity profile. The advantage of using a radial velocity profile boundary condition is that shorter inlets (15 mm, each containing 1,314 cells) could be used to save mesh and computational time. During the simulations second order discretization schemes and interpolations were used with different operators, as can be seen in Table 3. Time derivative used the implicit backward scheme. Other discretized operators used either Gauss or cell limited Gauss schemes.

Both simulation cases were set in a way to ensure that the maximum Courant number would stay in the range of 0.5. In that way the necessary condition for convergence was fulfilled. It was achieved by having a constant time step of 15 μ s. A constant time interval is important when Fourier Transformation is used on the results. Temperature and velocity data was sampled every 100 time steps. Probes were located on four vertical lines 1 mm outside the control rod stem shown in Fig. 5. Positions "N" and "S" were aligned along the cold inlets and positions "W" and "E" were aligned along the hot inlets. Each probing line contained 225 probes that were equally spread along the line which passed through the entire geometry.

3. Results and Discussion

3.1. First case, with the cold flow coming from below

In Fig. 6 the time series of the temperature 1 mm from the control rod stem at various vertical positions at probing location "N" is shown. To gain a better understanding of the vertical positions it should be noted that the position of the hot inlets is at $y = 0.6$ m. The non-dimensional temperature:

$$T^* = \frac{T - T_{cold}}{T_{hot} - T_{cold}}, \quad (12)$$

Table 2: Boundary conditions

	Wall	Inlet	Outlet
k_{SGS}	kqRWallFunction	fixedValue	inletOutlet
ν_{SGS}	nuSgsUSpaldingWallFunction	calculated	calculated
p	zeroGradient	zeroGradient	fixedValue
T	zeroGradient	fixedValue	inletOutlet
v	fixedValue	radialProfile, fixedValue	inletOutlet

Table 3: Discretization and interpolation schemes

	Discretization scheme	Interpolation scheme
$\frac{\partial}{\partial t}$	backward	
Gradient ∇	cellLimited Gauss	linear
Divergence $\nabla \cdot$	Gauss	filteredLinear2V limitedLinear linear
Laplacian Δ	Gauss	linear limited

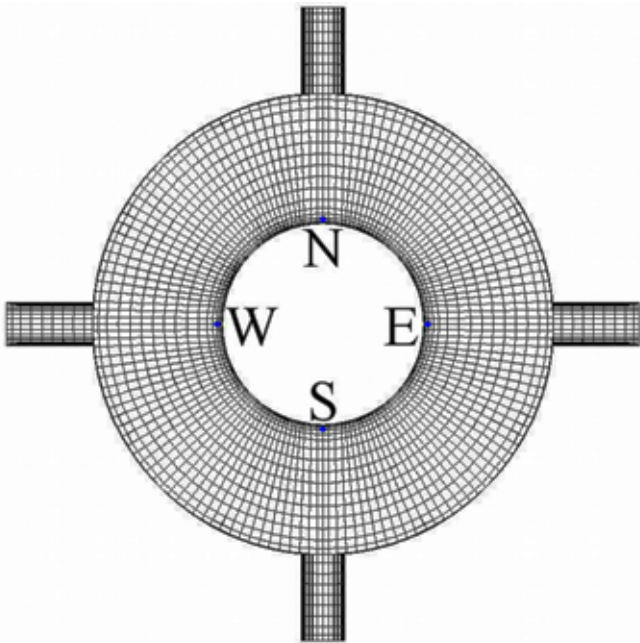


Figure 5: Probe locations (mesh viewed from above). The positions "W" and "E" were aligned along hot inlets

where T_{hot} and T_{cold} are the temperatures of the hot and the cold inlets, was used for displaying the results. One can observe a similar temperature behavior to that seen in the experiment carried out at Vattenfall Research & Development AB [3].

The overall mean temperature increases gradually upwards in the annular gap [3]. The maximum amplitude of the fluctuation corresponds to T^* varying from 0 to 0.8, and it was observed at the vertical position $y = 0.459$ m. The position corresponds to the location where the standard deviation of T^* has its maximum value, see Fig. 7. The low frequency temperature fluctuation of the order of 0.1 Hz can be most clearly observed at the position $y = 0.390$ m. Low frequent fluctuations of large amplitude are especially dangerous when it comes to thermal loads [3].

In Fig. 8 the time series of temperature is shown at various probing locations on the same vertical level. It can be observed that the instantaneous flow is asymmetric. It should be noted that "heat bullets" can mainly be found at the positions "N" and "S" (the stipulative definition, made of hot inlet jets penetrating into the colder flow, see Fig. 9. "Heat bullet" is visualized by making a wrapped slice of velocity at vertical position $y = 0.390$ m, which is colored by the temperature.). Fourier Transforming the data from Fig. 8, the temperature Fourier spectrum is obtained, see Fig. 14. One can see that the Fourier spectrum has its high amplitude "peaks" below 0.6 Hz. Distinctive "peaks" can be found at positions "N" and

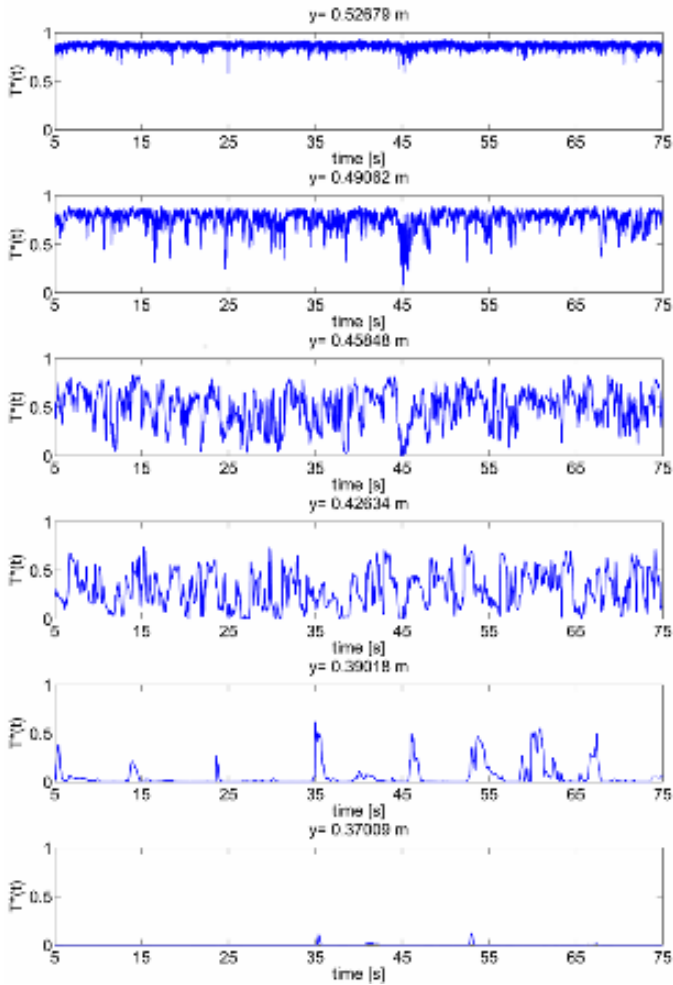


Figure 6: First case time series of temperature 1 mm from the control rod stem at various vertical positions at probing location "N". The hot inlets are located at $y = 0.6$ m

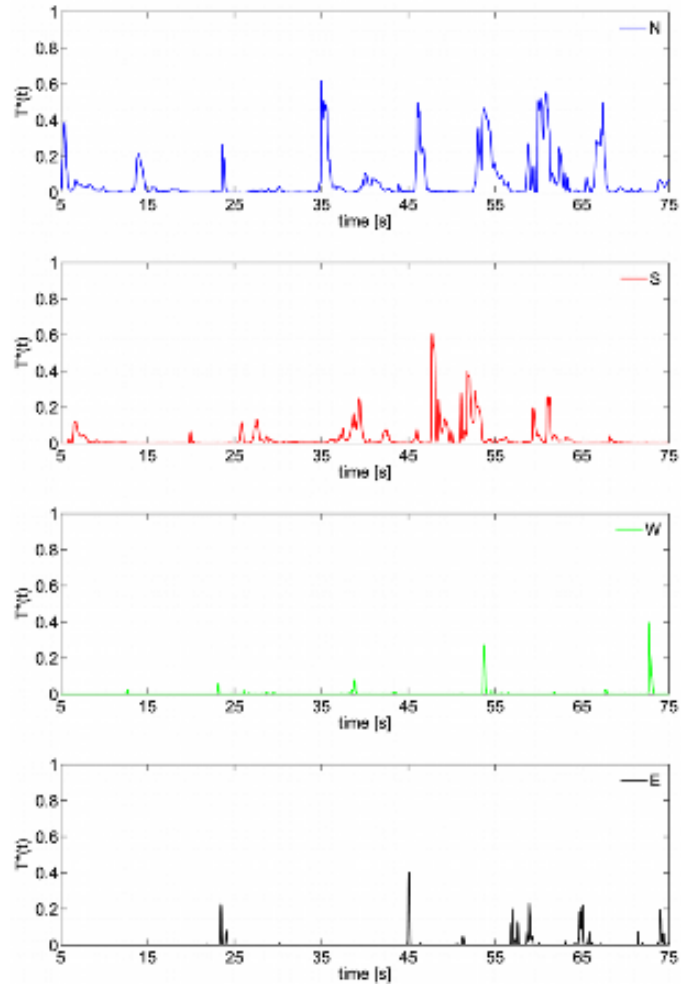


Figure 8: First case time series of temperature at vertical position $y = 0.390$ m at various probing locations

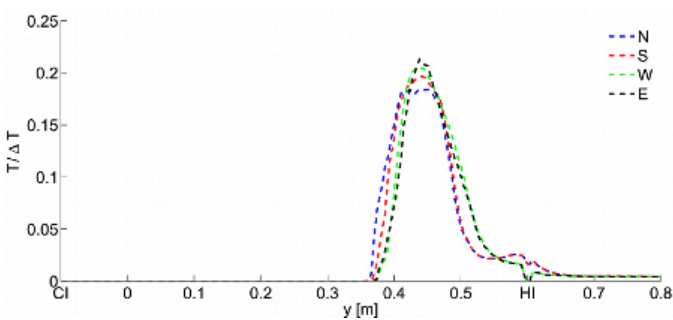


Figure 7: First case normalized temperature standard deviation at various probing locations ($\Delta T = 216$ °C)

"S", the most dominant being around 0.1 Hz. The "peak" near 0.01 Hz can be excluded because the simulation time was less than one full fluctuation at that frequency.

In Figs 7 and 10 the mean temperature and its stan-

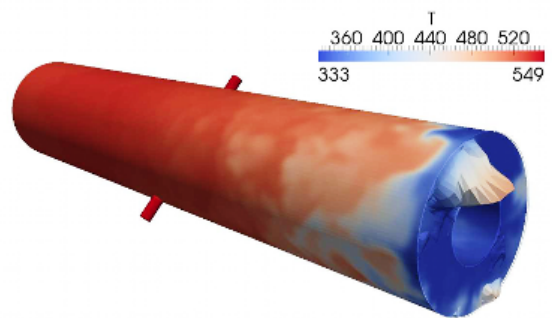


Figure 9: "Heat bullet" at vertical position $y = 0.390$ m at simulation time $t = 34.8$ s. First case geometry is shown at interval $y = [0.39018; 0.8]$ m

dard deviation can be seen at various probing locations as a function of the vertical position. In both figures the cold and the hot inlet locations are de-

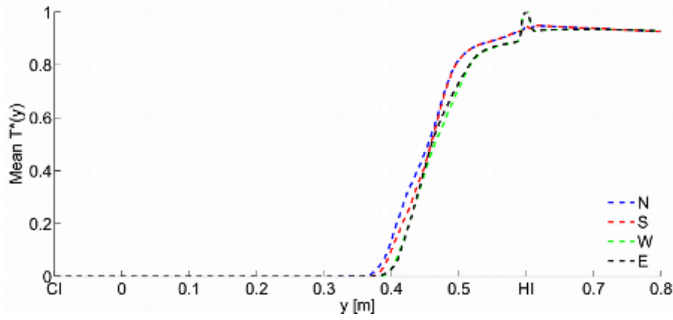


Figure 10: First case mean temperature at various probing locations

noted as "CI" and "HI", respectively. The length of the mixing region can be estimated to lie in the interval $y \in [0.350; 0.550]$, m. The estimation is done by studying the temperature standard deviation.

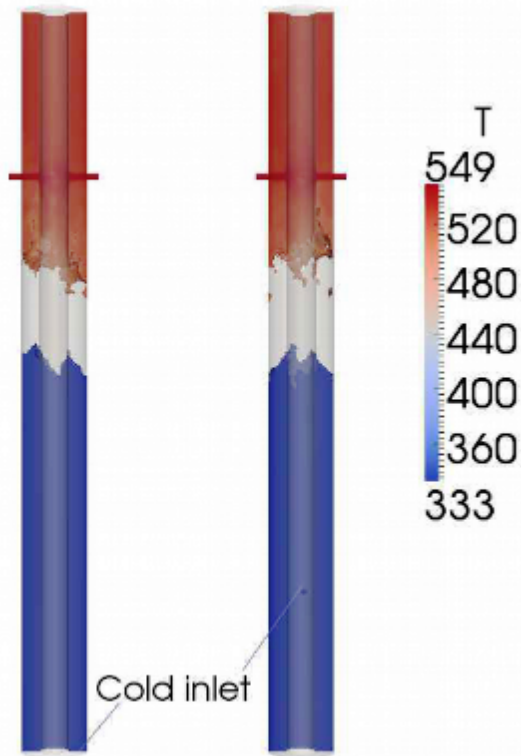


Figure 11: Visualization of the region where the temperature increases rapidly from 333 to 520 K. (cut view from symmetry plane)

In the mixing region positions "N" and "S" have a slightly higher mean temperature and lower standard deviation than positions "W" and "E". The mean temperature peak at "HI" for the positions "W" and "E" can be explained by the hot inlet jets hitting the stem wall at that position. The increase in tem-

perature is at its most rapid in the first 15 cm of the mixing region, see Fig. 11. Standard deviation stays below 50 K and it is 23% of the temperature difference between the hot and the cold inlet, see Fig. 7.

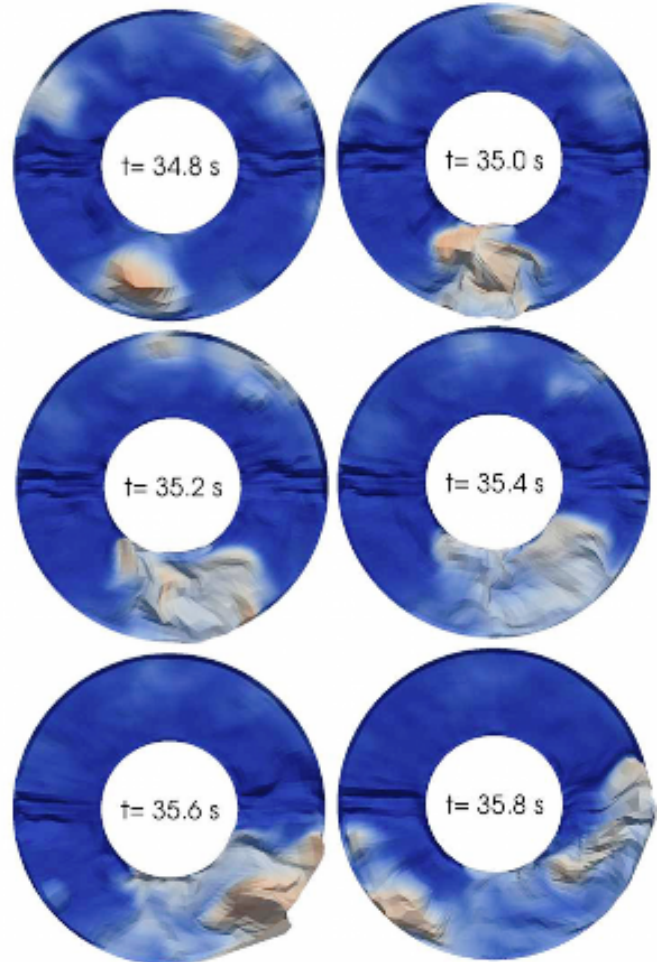


Figure 12: Time series of the flow movement in the annulus at vertical position $y = 0.390$ m

A secondary flow in the circumferential direction was observed in the mixing region, see Fig. 12. In Fig. 12 the anti-clockwise movement of "heat bullet" is seen from below and the pictures show wrapped slices of velocity colored by temperature. As the "heat bullet" penetrates into the colder flow with opposite direction it starts to rotate with an angular velocity of approximately $90^\circ/\text{s}$.

3.2. Second case, with cold inlets from the sides

The second geometry used differs only by the location of the cold inlet(s), see Fig. 11. The aim was

to see if cold inlets from the sides would affect the results. If cold jets had a large impact on the flow field then a possible remedy would be to use a perforated plate in the experiment to even out the flow from the jets in the annular gap.

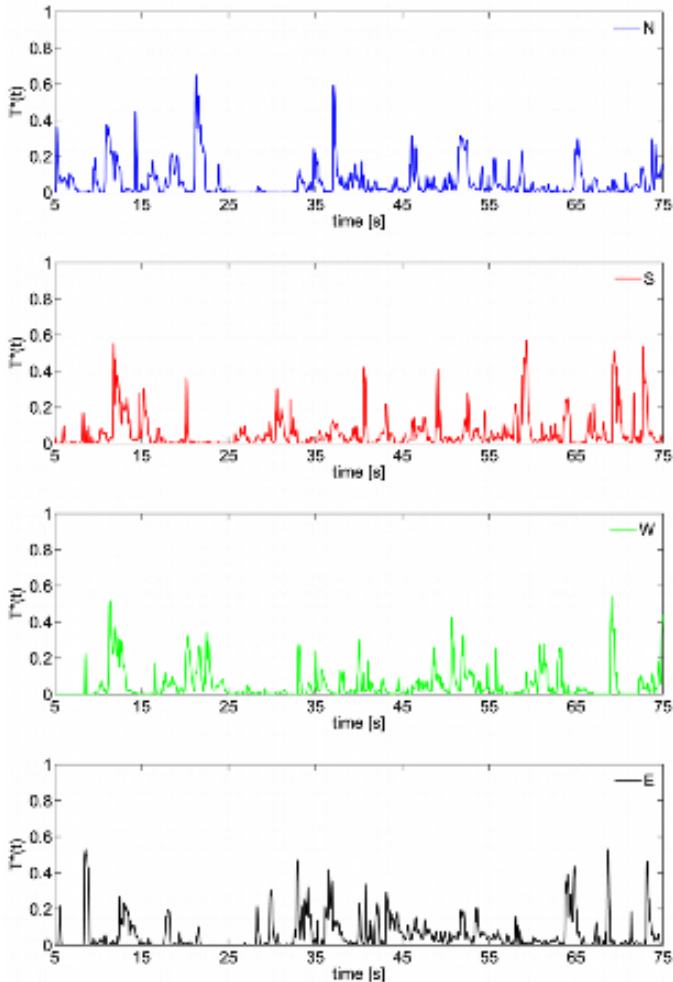


Figure 13: Second case time series of temperature at vertical position $y = 0.390$ m at various probing locations

A comparison of Figs 8 and 13 shows that there are considerably more "peaks" in the probe locations "W" and "E" when using the second geometry. These extra "peaks" are indirectly caused by the cold jets. While "heat bullets" are penetrating vertically downwards at positions "N" and "S", cold jets are moving vertically upwards at positions "W" and "E". Due to these movements flow rotation perpendicular to the vertical direction increases. Rotation of the "heat

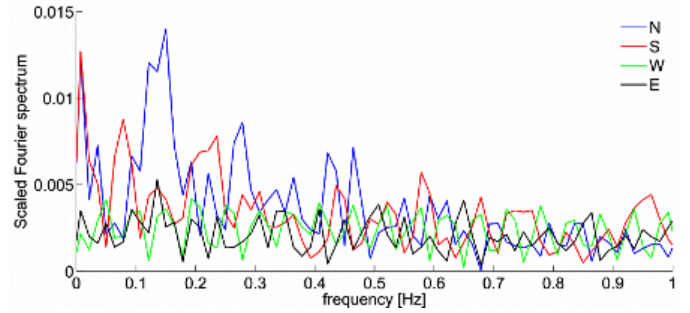


Figure 14: First case temperature Fourier spectrum at vertical position $y = 0.390$ m at various probing locations

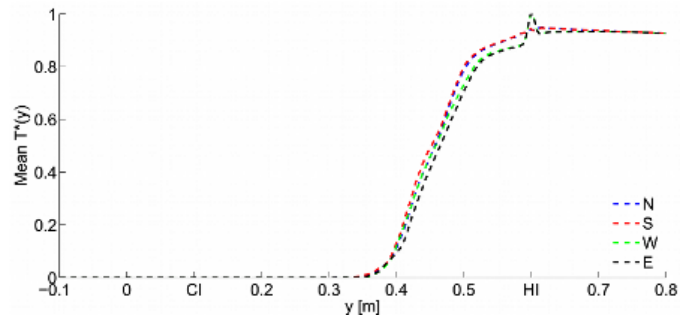


Figure 15: Second case mean temperature at various probing locations

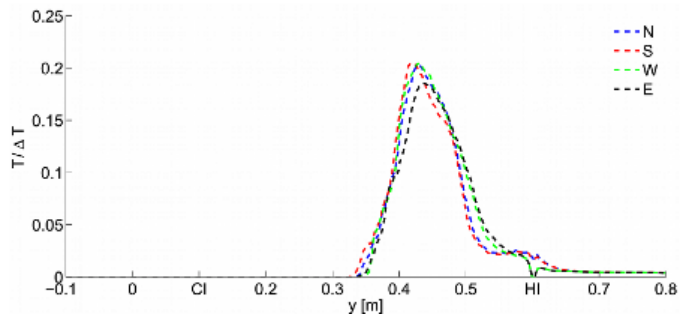


Figure 16: Second case normalized temperature standard deviation at various probing locations ($\Delta T = 216$ °C)

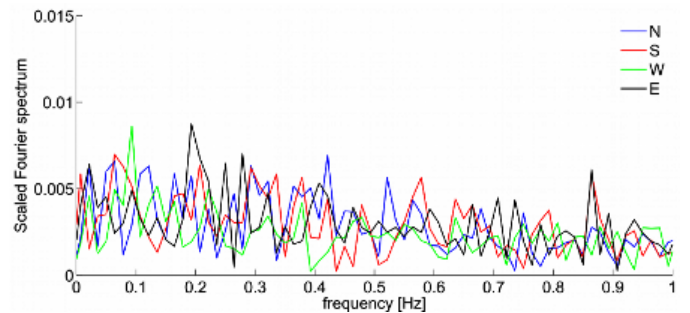


Figure 17: Second case temperature Fourier spectrum at vertical position $y = 0.390$ m at various probing locations

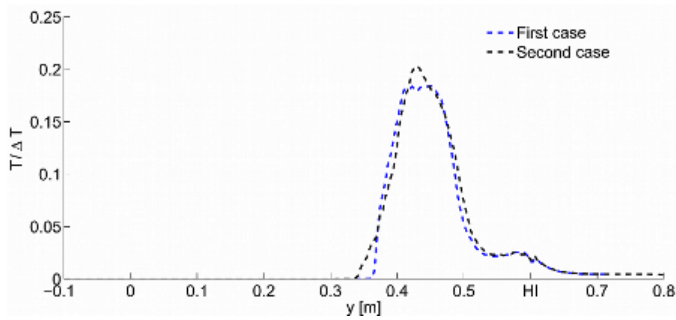


Figure 18: Normalized temperature standard deviation comparison at probing location "N" ($\Delta T = 216\text{ }^{\circ}\text{C}$)

bullets" causes temperature "peaks" at positions "W" and "E".

Figs 7, 11, 16 and 18 show that the mixing region $y \in [0.325; 0.550]$, m, is 2.5 cm longer than in the first case. The same tendency can be seen by comparing the mean temperatures, see Figs 10 and 15. In Fig. 17 one can see that the Fourier spectrum has its high amplitude "peaks" again below 0.6 Hz, but this time most dominant "peaks" are located at positions "W" and "E".

3.3. The most dangerous region

The length of the mixing region where the most dominant "peaks" in the temperature Fourier spectrum lie near the 0.1 Hz had to be estimated, because the low frequency fluctuations of large amplitude are especially dangerous with respect to thermal loads [3]. The estimation was done by investigating the temperature fluctuation amplitude and its Fourier spectrum. The purpose was to find the region where the scaled Fourier spectrum has a value over 0.007 near the frequency of 0.1 Hz and the amplitude is larger than 50 K.

The most dangerous region for the first case was $y \in [0.374; 0.406]$, m, and for the second case $y \in [0.370; 0.402]$, m. These regions have the same length and are shifted by 4 mm. The most dangerous region is less than 4 cm long.

4. Conclusions

The most important conclusions of this work are as follows:

- It was verified that the proposed geometry and flow conditions for the experiment give rise to the expected flow field. The simulations revealed that both considered geometries will generate low frequency temperature fluctuations of the order of 0.1...1 Hz in the mixing region. Sufficient data has been obtained to conclude that the patterns exist.
- The results indicate that the length of the mixing region is 23 cm. This is similar to the earlier experiment [3] and is large enough to be resolved in the experiment.
- The most dangerous region was found to be 4 cm long, and the dominant high amplitude temperature fluctuations there have a frequency of the order of 0.1 Hz.
- The two cases show that the cold inlets will affect the mixing region. If that is not desired a perforated plate could be installed.
- It can be observed that the instantaneous flow is asymmetric. Therefore it is not recommended to use only a quarter of the geometry, neither in CFD nor in the experiments, because with a quarter geometry the effect of rotating flow in the circumferential direction cannot be captured.
- The results support the idea that the cold inlets cannot be approximated as "flat" inlet, based on the differences observed between the two cases.

Acknowledgment

The financial support obtained from Forsmarks Kraftgrupp AB is gratefully acknowledged by the first author (R.P.). This work was carried out within the framework of DKC-TS, Distribuerat Kompetenscentra—Termohydraulik och Strömning, Vattenfall's initiative to exchange knowledge and experience between nuclear units in the field of thermal hydraulics and fluid mechanics.

References

- [1] U. S. N. R. Commission, Information on Control Rod Cracking Found at Swedish BWRs., accessed 5 February 2012 (Dec 2008).
- [2] H. Tinoco, H. Lindqvist, Thermal Mixing Instability of the Flow Inside a Control-Rod Guide Tube, Conference paper N13P1245, The 13th International Topical Meeting on Nuclear Reactor Thermal Hydraulics (NURETH-13), Kanazawa City, Ishikawa Prefecture, Japan (September 2009).
- [3] K. Angele, Y. Odemark, M. Cehlin, B. Hemström, C.-M. Högström, M. Henriksson, H. Tinoco, H. Lindqvist, Flow mixing inside a control-rod guide tube- Experimental tests and CFD simulations, Nuclear Engineering and Design 241 (2011) 4803–4812.
- [4] A. Bakker, Information on Computational Fluid Dynamics, Lecture 7- Meshing, accessed 13 April 2012 (Feb 2008).
- [5] S. N. Acharya, A general survey of hexahedral mesh generation, accessed 13 April 2012 (Jul 2004).
- [6] R. Courant, K. Friedrichs, H. Lewy, Über die partiellen Differenzgleichungen der mathematischen Physik, Mathematische Annalen 100 (1) (1928) 32–74.
- [7] E. de Villiers, The Potential of Large Eddy Simulation for the Modeling of Wall Bounded Flows, PhD dissertation, Imperial College of Science, Technology and Medicine, Department of Mechanical Engineering (Jul 2006).
- [8] ANSYS Inc., ICEM CFD Help Manual, accessed 11 September 2013 (Nov 2011).
- [9] K. Abe, A hybrid LES/RANS approach using an anisotropy-resolving algebraic turbulence model, International Journal of Heat and Fluid Flow 26 (2005) 204–222.
- [10] Y. Gong, F. X. Tanner, Comparison of RANS and LES Models in the Laminar Limit for a Flow Over a Backward- Facing Step Using OpenFOAM, Conference paper, Nineteenth International Multidimensional Engine Modeling Meeting at the SAE Congress, Detroit, Michigan, USA (Apr 2009).
- [11] L. Davidson, Fluid mechanics, turbulent flow and turbulence modeling, Chalmers University of Technology, Goteborg, Sweden (Nov 2011).
- [12] OpenFOAM Foundation, OpenFOAM User Guide, accessed 15 April 2012 (Dec 2011).
- [13] OpenFOAMWiki, The SIMPLE algorithm in OpenFOAM, accessed 14 April 2012 (Mar 2010).
- [14] OpenFOAMWiki, The PISO algorithm in OpenFOAM, accessed 14 April 2012 (Nov 2009).
- [15] T. Ming, J. Zhao, Large-eddy simulation of thermal fatigue in a mixing tee, International Journal of Heat and Fluid Flow 37 (2012) 93–108.
- [16] N. Edh, radialProfile (2012).
- [17] OpenFOAMWiki, BuoyantBoussinesqPisoFoam, accessed 14 April 2012 (Jun 2010).
- [18] H. Jasak, Error Analysis and Estimation for the Finite Volume Method with Application to Fluid Flows, PhD dissertation, University of London, Department of Mechanical Engineering (Jun 1996).
- [19] J. Westin, P. Veber, L. Andersson, High-Cycle Thermal Fatigue in Mixing Tees: Large-Eddy simulations Compared to a New Validation Experiment, Conference paper ICONE16-48731 pp. 515-525, 16th International Conference on Nuclear Engineering (ICONE16), Orlando, Florida, USA (May 2008).